

Accurate relativistic observables from postprocessing light cone catalogsChi Tian^{1,*}, Matthew F. Carney¹, James B. Mertens¹, and Glenn Starkman²¹*Department of Physics and McDonnell Center for the Space Sciences, Washington University,
St. Louis, Missouri 63130, USA*²*CERCA/ISO, Department of Physics, Case Western Reserve University,
10900 Euclid Avenue, Cleveland, Ohio 44106, USA*

(Received 18 October 2021; accepted 23 January 2022; published 10 March 2022)

We introduce and study a new scheme to construct relativistic observables from postprocessing light cone data. This construction is based on a novel approach, LC-METRIC, which takes general light cone or snapshot output generated by arbitrary N -body simulations or emulations and solves the linearized Einstein equations to determine the spacetime metric on the light cone. We find that this scheme is able to determine the metric to high precision, and subsequently generate accurate mock cosmological observations sensitive to effects such as post-Born lensing and nonlinear integrated Sachs-Wolfe contributions. By comparing to conventional methods in quantifying those general relativistic effects, we show that this scheme is able to accurately construct the lensing convergence signal. We also find that the accuracy of this method in quantifying the integrated Sachs-Wolfe effects in the highly nonlinear regime outperforms conventional methods by an order of magnitude. This scheme opens a new path for exploring and modeling higher-order and nonlinear general relativistic contributions to cosmological observables, including mock observations of gravitational lensing and the moving lens and Rees-Sciama effects.

DOI: [10.1103/PhysRevD.105.063511](https://doi.org/10.1103/PhysRevD.105.063511)**I. INTRODUCTION**

Observations of our Universe across cosmological distances offer us an ideal grounds for testing the behavior of long-standing physical theories, alongside new ones, ranging from signatures of new primordial phenomena [1–5], to models of dark energy [6–10], to general relativity (GR) itself [11,12]. On the other hand, it is often on small scales—the distances considerably smaller than our cosmological horizon on which nonlinear growth of structure occurs—that we have been able to perform our most precise measurements. Upcoming experiments, such as CMB-S4 [13] and the Vera Rubin Observatory (formerly LSST) [14] will begin to provide us with a view of the Universe that encompasses both of these regimes. Together, maps of the cosmic microwave background (CMB), of the large-scale galaxy distribution, and of other tracers of matter in the Universe are expected to be of sufficient sensitivity and volume that we can measure or constrain a variety of the subtle effects that leave an imprint on ultralarge scales [15].

Sophisticated, accurate theoretical predictions are essential for optimal analysis of observations at this level of precision, and large suites of simulations are often required to make statistically meaningful predictions. To this end, a variety of procedures designed to generate accurate mock observations without running more expensive simulations

of structure formation have been proposed and explored, with varying degrees of success [16–22]. These emulators can efficiently incorporate nonlinear physics in cosmological models, and can further be used to generate a variety of observations consistently in order to study e.g. cross-correlations or to test procedures such as tomographic reconstruction. However, methods for incorporating light cone projection effects in mock observations are underdeveloped, especially at a nonlinear level. For unbiased extraction of cosmological parameters, especially arising from information contained within cross-correlations and higher-order statistics, it will be necessary to simultaneously model non-Newtonian, horizon-scale effects alongside subtle yet still important small-scale nonlinear physics. Addressing this has been a focus of a number of studies, which have found different statistics and inferred cosmological parameters to be sensitive to such effects to various degrees [23–28].

Accurately predicting observable properties of our Universe requires accurate knowledge of the spacetime metric through which information has propagated to us—in particular, knowledge of this metric on our past light cone. The idea of determining the metric on the past light cone from observations has been explored in a large-scale setting in several works [29–31]. In this work we introduce a novel method LC-METRIC (light cone metric restoration) for extracting the metric on our past light cone from either a mock density field on the light cone, or a series of constant-

*chit@wustl.edu

time “snapshots” from simulations, and subsequently computing observable quantities. We focus on the ability of this method to act as a postprocessing procedure for the output of both standard Newtonian N -body simulations and cosmic emulators, especially those for which a small number of time steps may have been taken and so recovery of the metric and its time derivative is less straightforward. Once recovered, we can use the metric to subsequently account for gravitational effects in generated mock observations, including post-Born corrections to gravitational lensing and nonlinear contributions to the integrated Sachs-Wolfe (ISW) effect.

Nonlinear corrections to lensing and the ISW effects have been examined in literature using a variety of schemes in which approximations are employed to circumvent the need to determine the metric and its derivatives. However, as accurately modeling observables will be important both at low and high redshift, on small and large scales, and for a number of observables including the CMB temperature and polarization, and galaxy power spectra, it will be important to consistently and correctly incorporate both nonlinear and large-scale light-cone-projection corrections [32–34]. The nonlinear ISW effect itself can be decomposed into several contributions, including the Rees-Sciama and moving-lens effects [35], which are expected to be detectable by future experiments with high signal-to-noise [13]. Gravitational lensing itself is perhaps better studied in literature, including nonlinear contributions [36–46]. Our approach in modeling these effects will be to first validate our approach, and then to produce lensing and ISW maps that are both consistent with other observables and also include nonlinear contributions.

For weak-lensing simulations, previous studies have employed an approximate thin-lens scheme using multiple planes or spheres of mass [31,37,39–41,43,44,47–49]. (See also [50] for a comprehensive review and code comparison of some existing weak-lensing simulations.) While some of these studies rely on the Born approximation, assuming unperturbed photon geodesics, other studies beyond the Born approximation find good agreement depending on the statistic and scales in question ([39,43,51–53]). In contrast to lensing, modeling the ISW effect requires knowledge of the time derivative of the metric potential, which makes its calculation more computationally challenging. This is especially true when computing the ISW signal in the highly nonlinear regime, and when postprocessing simulation data. Various techniques have been studied in past literature to this end [54–59]. These all require either output from a large number of snapshots or on-the-fly ray tracing, and so are not directly applicable as a postprocessing step, which is especially important for fast emulators.

Here, we work to establish a numerical framework in which we can robustly compute nonlinear ISW and post-Born lensing contributions from Newtonian light cone simulation or emulator output. Rather than considering

specific effects or terms in such a calculation, we will aim to extract the full nonlinear ISW and lensing contributions. We attempt to remain agnostic as to the simulation output; our method can be applied to a variety of sources, ranging from N -body codes such as GADGET [60] to emulators that provide light cone output such as L-PICOLA [17]. We will primarily rely upon the latter of these codes in this work, especially as output from COLA methods will converge to that of a standard N -body simulation in the limit of a large number of time steps. We compare our approach to conventional approximate approaches based on simulation snapshots or light cones, and compare the requirements for numerical convergence between our method and other approaches. We find that our approach to modeling the weak-lensing power spectrum agrees well with other approaches that utilize the Born approximation, although we do note some differences. Importantly, we find that our scheme significantly outperforms conventional schemes when modeling the ISW effect in the highly nonlinear regime.

We expect our results and framework to be relevant for modeling of higher-order and relativistic effects in cosmological observables such as the moving-lens and Rees-Sciama (nonlinear ISW) effects [35], higher-order contributions to observations of the CMB including e.g. post-Born corrections or lensing of the Sunyaev Zeldovich (SZ) signal itself. While some of these corrections have been studied and may be detectable by upcoming experiments [13,61,62], various higher-order effects have yet to be examined in detail—one of our goals is to initiate a study in this direction. Our code has been made public and can be found at [63].

This paper is structured as follows. In Sec. II, we review linearized GR theory, and describe our scheme to recast the linearized GR equations into a hyperbolic form on the past light cone. We then introduce our numerical method for solving these equations, which employs a multigrid technique to relax these equations and determine the Newtonian potential and its derivatives. In Sec. III, we calculate cosmological observables, including the weak-lensing and the (nonlinear) ISW effects, from the metric on the past light cone, and compare them with some conventional approximate methods. We summarize and conclude in Sec. IV.

II. METHODOLOGY

A. Linearized GR equations

The scheme we present here is based on a linearized treatment of the spacetime metric in Newtonian gauge (see e.g. [64]). In this work, we will assume there is no anisotropic stress so the two Newtonian potentials are equal, although this assumption may be relaxed in a more general setting. We further do not study the impact of vector or tensor perturbations, although these may be treated by a similar procedure. Given these approximations, the perturbed metric in Newtonian gauge can be written as

$$ds^2 = a^2[(1 + 2\Phi)d\tau^2 - (1 - 2\Phi)\delta_{ij}(dx^i dx^j)], \quad (1)$$

with Φ as the Newtonian potential. The comoving Hubble parameter \mathcal{H} is proportional to the Hubble parameter H as $\mathcal{H} = aH$, and, in a universe containing just dust and vacuum energy, it evolves according to the Friedmann equation

$$\mathcal{H}^2 = \mathcal{H}_0^2 a^2 (\Omega_m a^{-3} + \Omega_\Lambda), \quad (2)$$

where \mathcal{H}_0 represents the current expansion rate. The background homogeneous stress tensor can be written

$$\bar{T}^\mu{}_\nu = (\bar{\rho} + \bar{P})\bar{U}^\mu \bar{U}_\nu - \bar{P}\delta^\mu_\nu, \quad (3)$$

where $\bar{U}_\mu = a\delta_\mu^0$ and $\bar{U}^\mu = a^{-1}\delta_0^\mu$. The perturbation to the matter content $\delta T^\mu{}_\nu$ is

$$\delta T^0_0 = \bar{\rho}\delta, \quad (4)$$

$$\delta T^i_0 = (\bar{\rho} + \bar{P})v^i, \quad (5)$$

$$\delta T^0_j = -(\bar{\rho} + \bar{P})v_j, \quad (6)$$

$$\delta T^i_j = -\delta P\delta^i_j + \Pi^i_j, \quad (7)$$

where δ is defined $\delta \equiv (\rho - \bar{\rho})/\bar{\rho}$ and v_i denotes the peculiar velocity field. Ignoring the anisotropic stress tensor Π^i_j and keeping the linear terms in the metric and the matter field, the linearized Einstein equations can be written as

$$\nabla^2\Phi - 3\mathcal{H}(\Phi' + \mathcal{H}\Phi) = 4\pi G a^2 \bar{\rho}\delta, \quad (8)$$

$$\partial_i(\Phi' + \mathcal{H}\Phi) = -4\pi G a^2 (\bar{\rho} + \bar{P})v_i, \quad (9)$$

$$\Phi'' + 3\mathcal{H}\Phi' + (2\mathcal{H}' + \mathcal{H}^2)\Phi = 4\pi G a^2 \delta P. \quad (10)$$

The prime symbol denotes a time derivative with respect to the conformal time τ . We set the pressure perturbation, δP , to zero under the collisionless-particle approximation in the remainder of the paper.

B. Connecting Newtonian N -body simulations to GR

The vast majority of simulations of large-scale structure formations are performed within a Newtonian gravity framework, rather than a general relativistic setting. While there are exceptions [65–71], in general this necessitates a translation between Newtonian simulation output and the corresponding general-relativistic quantities in the appropriate gauge. One promising approach to reconciling this discrepancy involves reinterpreting the input and output to standard Newtonian codes in gauges specially developed for this purpose [66]. Another straightforward

option, which we employ here, is to transform the output of Newtonian codes to approximately agree with a relativistic interpretation as proposed in [72]. The following dictionary maps output from Newtonian simulations to output in Newtonian gauge,

$$\Phi = \Phi_{\text{sim}}, \quad (11)$$

$$\vec{v} = \vec{v}_{\text{sim}}, \quad (12)$$

$$\vec{x} = \vec{x}_{\text{sim}} + \delta\vec{x}_{\text{in}}. \quad (13)$$

To find the value of corrections $\delta\vec{x}_{\text{in}}$ to particle positions, we can simply solve the equation [72]

$$\nabla \cdot \delta\vec{x}_{\text{in}} = 5\Phi_{\text{in}}, \quad (14)$$

where Φ_{in} is the gravitational potential determined when setting initial conditions. Our postprocessing scheme uses this dictionary to correct particle positions given by N -body simulations. We also note that the (Newtonian) density contrast δ is subject to a GR correction

$$\delta = (1 + 3\Phi)\delta_{\text{sim}} = (1 + 3\Phi)\bar{n} \sum_i \delta_D^{(3)}(\mathbf{r} - \mathbf{r}_i) - 1, \quad (15)$$

where \bar{n} is the average particle density, and $\delta_D^{(3)}(\mathbf{r})$ is the 3D Dirac delta function. In the test cases we present in this paper, the GR corrections are only appreciable at the largest scales.

C. Solving Einstein's equations on the light cone

Our past light cone can be thought of as a sequence of nested spherical shells. We will therefore work in a spherical polar coordinate system (r, θ, ϕ) , where r is the comoving distance and θ and ϕ are the azimuthal and polar angles, respectively. We further employ the coordinate transformations.

$$\tau \rightarrow \eta, \quad (16)$$

$$r + \tau \rightarrow w, \quad (17)$$

under which varying η corresponds to considering future/past null coordinate cones, while $w = \text{const}$ corresponds to the surface of a specific null coordinate cone. We also manually set $w = 0$ for past light cone of the observer at $z = 0$. The coordinate system after this transformation is equivalent to “geodesic light cone coordinates” to leading order [73–75]. To transform the equations of motion (EOM) Eqs. (8) to (10) into the coordinate system (η, w, θ, ϕ) , we can rewrite the EOM Eqs. (8) to (10) in standard spherical coordinates (τ, r, θ, ϕ) and use the following transformation relations for partial derivatives

$$\partial_\tau \rightarrow \partial_\eta + \partial_w, \quad (18)$$

$$\partial_r \rightarrow \partial_w, \quad (19)$$

$$\partial_\tau^2 \rightarrow \partial_\eta^2 + 2\partial_\eta \partial_w + \partial_w^2, \quad (20)$$

$$\partial_r^2 \rightarrow \partial_w^2. \quad (21)$$

These are derived directly from the coordinate transformations relations, and can be used to rewrite the EOMs in the new coordinate system,

$$\begin{aligned} \ddot{\Phi} = & -\frac{2}{r}\Pi + 2\mathcal{H}\Pi - 2(\dot{\mathcal{H}} - \mathcal{H}^2)\Phi + 4\pi G a^2 \bar{\rho} \delta \\ & + 3 \times (4\pi G a^2 \bar{\rho} \Phi) - \frac{\nabla^{(2)}\Phi}{r^2} + 2 \times 4\pi G a^2 \bar{\rho} v_r, \end{aligned} \quad (22)$$

$$\dot{\Xi} = -2\mathcal{H}\Xi - \mathcal{H}\Omega - (2\dot{\mathcal{H}} + \mathcal{H}^2)\Phi + 4\pi G a^2 \bar{\rho} v_r. \quad (23)$$

Here, we have defined some shorthands for partial derivatives in the new coordinates,

$$\dot{X} \equiv \frac{\partial X}{\partial \eta}, \quad X' \equiv \frac{\partial X}{\partial r} = \frac{\partial X}{\partial w} \quad (24)$$

for a field X , and also shorthands for several new variables,

$$\Omega \equiv \dot{\Phi}, \quad \Pi \equiv \Phi', \quad \Xi \equiv \partial_\tau \Phi = \Pi + \Omega. \quad (25)$$

Equations (22) and (23) comprise a second-order linear partial differential equation (PDE) coupled to a first order PDE. We discretize the solution onto a spherical mesh by discretizing the comoving time direction $\eta(\tau)$ uniformly, and discretizing angular directions (θ, ϕ) according to the HEALPix convention (see Appendix A 2 for more detail). Under this discretization, the density contrast δ and the radial velocity fields v_r can be extracted from particle data using any preferred deposition scheme, such as nearest-grid-point (NGP) or cloud-in-cell (CIC) deposition. The weights we use for radial grids correspond to standard CIC weights, while the angular weights are given by the HEALPix `get_interpol` function. To calculate the angular Laplacian term $\nabla^{(2)}\Phi$ in Eq. (22), we also employ HEALPix to perform spherical harmonics transformations to compute the spherical harmonic coefficients a_{lm} for all terms in the Eqs. (22) and (23) under the convention

$$a_{lm} = \frac{4\pi}{N_{\text{pix}}} \sum_{p=0}^{N_{\text{pix}}-1} Y_{lm}^*(\theta_p) f(\theta_p). \quad (26)$$

In harmonic space, $\nabla^{(2)}\Phi$ can be simply represented by $\ell(\ell+1)\Phi_{lm}$, where Φ_{lm} are the spherical harmonic coefficients of Φ . For radial derivatives in Eqs. (22) and

(23), we employ a second-order finite-differencing method to calculate them.

The strategy employed to solve this boundary value problem is to use a relaxation scheme to solve Eq. (22) and direct time integration to solve Eq. (23) (see Appendix A 2 for more detail). To this end, two boundary conditions for Φ and one boundary condition for Ξ are required. These data can be estimated from two snapshots at boundaries. For example, the Φ field on the boundaries can be quantified by combining the Friedmann equation Eq. (2) with the Poisson equation for gravity. The resulting Φ field on boundary snapshots in Fourier space can be calculated from

$$\Phi(\mathbf{k}, \tau) = -\frac{3}{2} \left(\frac{H_0}{k} \right)^2 \Omega_m \frac{\delta(\mathbf{k}, \tau)}{a}. \quad (27)$$

Also, by plugging in the continuity equation $\dot{\delta}(\mathbf{k}, \tau) + i\mathbf{k} \cdot \mathbf{p}(\mathbf{k}, \tau) = 0$ in Fourier space, we have the value for Ξ on boundary snapshots

$$\Xi \equiv \frac{\partial \Phi}{\partial \tau}(\mathbf{k}, \tau) = -\frac{3}{2} \left(\frac{H_0}{k} \right)^2 \Omega_m \left[\frac{H}{a} \delta(\mathbf{k}, \tau) + \frac{i\mathbf{k} \cdot \mathbf{p}(\mathbf{k}, \tau)}{a} \right], \quad (28)$$

where $\mathbf{p}(\mathbf{k}, \tau)$ is the Fourier transform of $[1 + \delta(\mathbf{x}, \tau)]\mathbf{v}(\mathbf{x}, \tau)$, and the velocity field $\mathbf{v}(\mathbf{x}, \tau)$ is again extracted from the CIC or NGP schemes on the boundary snapshot. After collecting the Φ and Ξ fields on boundary snapshots, we project the data onto a HEALPix sphere through linear interpolations. Replications of the snapshots are necessary for setting the boundary data at higher redshift.

After imposing boundary conditions at higher and lower redshifts [76], we use a relaxation scheme to solve for each spherical harmonic coefficient in each radial bin. When the size of voxels on spherical grids approximately matches the voxels from Cartesian grids of N -body simulations, using too many spherical grids will prevent an ordinary relaxation technique (e.g. Newton's method) from converging to the true solutions of Eqs. (22) and (23) in a practical amount of time. We therefore employ a multigrid method [77], which builds a hierarchy of the computational grids to accelerate the relaxation procedure. We find that employing the multigrid method will result in approximately a 10x speedup compared to the conventional Newton relaxation method. The relaxation process is accomplished by repeating V-cycle iterations (see Appendix A 2 for more details about the relaxation scheme, the multigrid method, and the V-cycle), and an example for the relaxation procedure for the reconstructed potential Φ_{LC} at $z = 0.3$ is shown in Fig. 1. The Φ_{LC} quickly converges to the potential on the snapshots Φ_{snap} at the same redshift as more and more V-cycle iterations are performed. Further details about the convergence of the solver can be found in Appendix B 1.

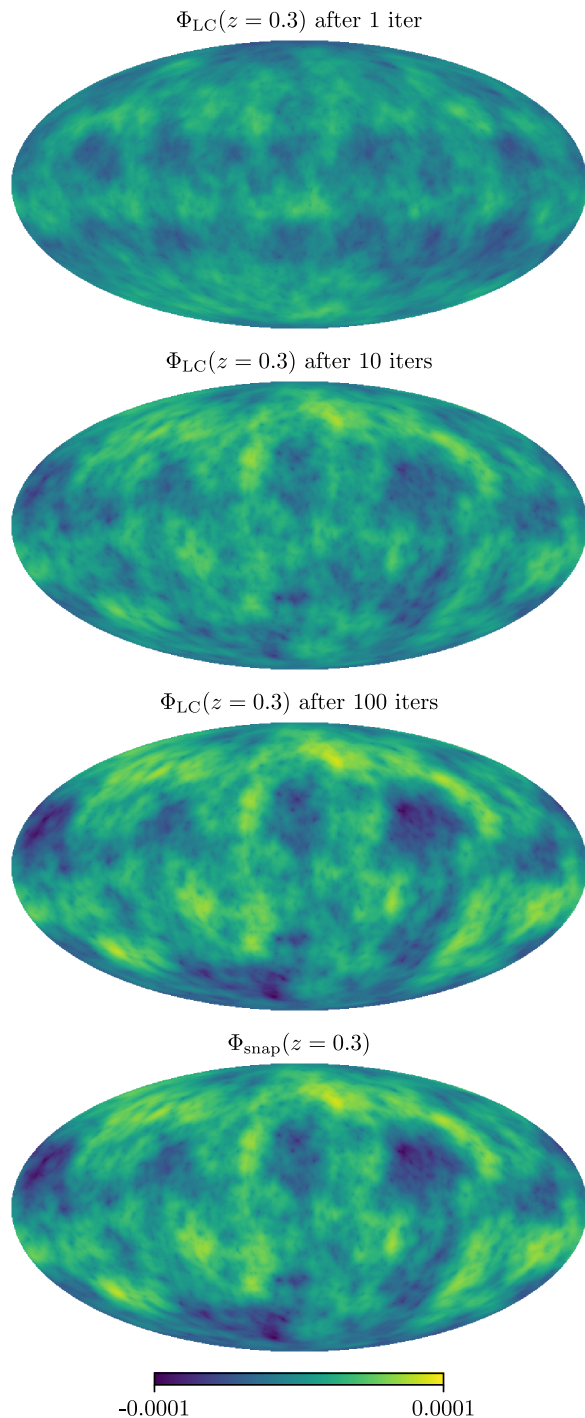


FIG. 1. Comparison of a Φ snapshot at $z = 0.3$ between the direct snapshot output Φ_{snap} and the restored Φ_{LC} after 1, 10, and 100 iterations (No. of V-cycles).

D. Simulation data and light cone construction

To validate our metric reconstruction procedure, we will focus on postprocessing simulated light cone data, which is most accurately constructed through on-the-fly interpolation during N -body simulations. However, as the most common output format of N -body simulations is snapshots,

our scheme is also designed to be able to work with light cone data restored from snapshots. To validate the LC-METRIC reconstruction scheme, we run a suite of dark-matter-only N -body simulations using the L-PICOLA code [78], and subsequently use LC-METRIC to postprocess its output. L-PICOLA implements the COLA method, a reference formulation using second-order Lagrangian perturbation theory to quickly solve the Newton-Vlasov system [79]. A significant speed-up compared to conventional particle-mesh method is typically found, especially on large scales; further, this method will produce equivalent results to standard N -body codes for sufficiently small time steps [78].

Our simulations are carried out with 1024^3 dark-matter particles in a periodic box with side length $L = 1024h^{-1}$ Mpc, corresponding to a particle mass of approximately $10^{11} M_{\odot}$. The density field of dark-matter particles is CIC deposited onto 1024^3 Cartesian grids, and forces are computed using fast Fourier transforms. The background cosmology is chosen to be a flat Λ CDM model with parameters $\Omega_m = 0.31$, $\Omega_{\Lambda} = 0.69$, $h = 0.69$, $\sigma_8 = 0.83$, and $n_s = 0.96$. Initial conditions for the simulations are generated based on a linear transfer function computed using CLASS with matching cosmological parameter values [80] at $z = 9$.

As the LC-METRIC scheme supports both light cone N -body data and snapshots data, we run the L-PICOLA code twice under light cone mode and normal (snapshot) mode to generate corresponding outputs with the same random seed. When snapshots data is given, we construct the light cone data from the snapshots by extrapolating particle positions according to their velocities and calculating their intersections with the light cone. We also replicate our computational box to cover the entire light cone. Although this replication procedure will result in artifacts on large scales, as a proof of concept for our metric-recovery scheme, we will primarily focus on whether the mock light cone metric can be correctly computed from a given density field. Further details of our scheme for constructing light cone data from snapshots is described in Appendix C. By choosing the two boundaries slices to be at redshifts $z \approx 0.03$ and $z \approx 0.52$, we construct our light cone metric extending between these redshifts. Note that even though we test our code by postprocessing L-PICOLA N -body output, our scheme will work with generic light cone or snapshot data that contains particle positions and peculiar velocities.

When constructing a light cone from snapshots, a useful technique supported by LC-METRIC is the “thick” light cones scheme. As shown in Fig. 2, by shifting the original light cone in the time direction, we construct two auxiliary light cones. The amount by which the light cone is shifted is set to be equal to the radial resolution of light cones, so that the voxels both have the same conformal radius r , and are aligned in the time direction. Under this configuration, the partial derivative with

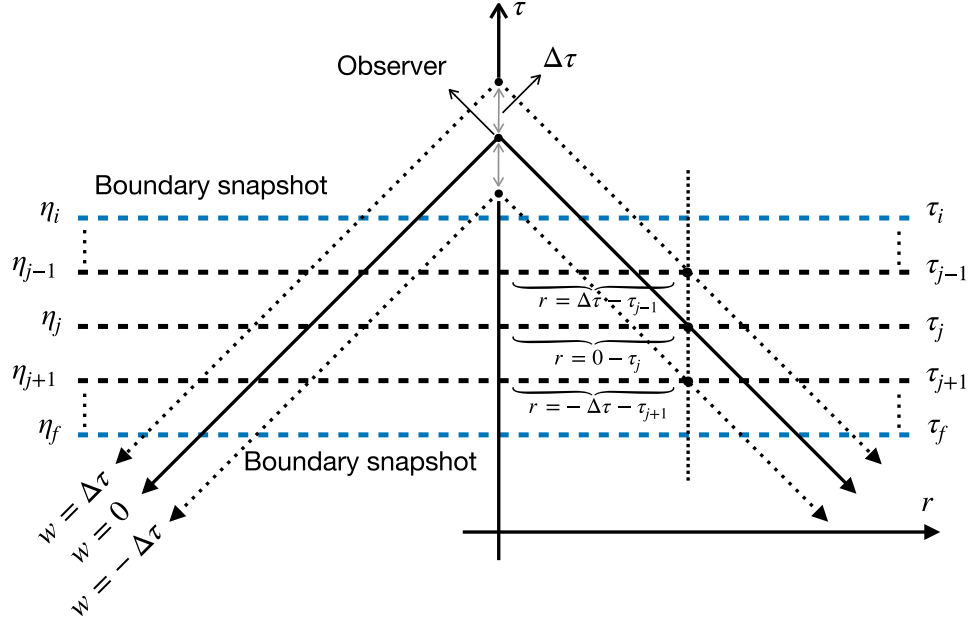


FIG. 2. Illustration of the construction of “thick” light cones, which are the light cones containing information between the dotted lines in the figure. They are computed by obtaining additional light cone data for observers separated positively and negatively in time by a conformal time $\Delta\tau$, which is also equal to the radial resolution of the light cone mesh. The snapshots are represented by horizontal dashed lines, and the top and bottom blue lines are boundary snapshots. The three dots vertically aligned on snapshots representing three mesh grids on each light cone, as an example, have equal spatial coordinates.

respect to conformal time of any field can be calculated directly using the second-order finite-differencing scheme. The “thick” light cones scheme will also facilitate the calculation when light rays deviate from the “thin” light cone when tracing the null geodesics precisely.

After reading in light cone data, we deposit particle masses and radial peculiar velocities onto our spherical grids, which have radial resolution $N_\eta = 1024$ and angular resolution corresponding to $N_{\text{side}} = 512$. The number of radial grids is chosen to ensure the radial resolution of the light cone $\Delta\eta = \Delta r$ approximately matches the Cartesian resolution Δx ; the angular resolution is set to make sure that most of the spherical-coordinate voxels are larger than the Cartesian voxels to avoid oversampling. Appendix B discusses how the cosmological observables vary with the choice of resolution.

We will further need to account for power suppression due to the implicit convolution associated with depositing particle masses onto grids (either through CIC or NGP). We deconvolve the grids using corresponding window functions to restore a true representation of the density field. For N -body simulation data from L-PICOLA, we use a window function [81]

$$W(\mathbf{k}) = \left[\text{sinc}\left(\frac{\pi k_x}{2k_N}\right) \text{sinc}\left(\frac{\pi k_y}{2k_N}\right) \text{sinc}\left(\frac{\pi k_z}{2k_N}\right) \right], \quad (29)$$

where k_N is the Nyquist frequency, and the underlying density field $\delta^m(\mathbf{k})$ is calculated from

$$\delta^m(\mathbf{k}) = W(\mathbf{k})^{-p} \delta(\mathbf{k}), \quad (30)$$

where $\delta(\mathbf{k})$ is the density field obtained from mass depositing scheme directly, and p is 1 and 2 for the NGP and CIC schemes, respectively.

Similar to the NGP or the CIC particle-deposition procedures on Cartesian grids, when depositing particle masses onto the HEALPix grids, a similar window function $W_\ell \approx \text{sinc}(\ell\Delta\theta/2\pi)$ should be considered, and the density fields on the HEALPix grids also need to be corrected by

$$\delta_l^m = W_l^{-p} \delta_l, \quad (31)$$

where p is similarly 1 and 2 for the NGP and CIC depositing schemes. In this study, we choose to scale all the spherical-harmonics coefficients in the density and velocity fields according to the approximate window function available through HEALPix.

A smoothing procedure is also introduced for the density fields on HEALPix grids through the size of individual HEALPix pixels possibly being significantly smaller than the resolution of an N -body simulation at low comoving radius. Unless specified, we convolve the density and velocity fields on HEALPix grids with a Gaussian smoothing kernel with half-max width

$$\theta_s = \Delta x/2r, \quad (32)$$

where Δx is the resolution of the N -body simulation and r is the comoving radius at each specific spherical shell. The inner shell (at lower redshift) will have a larger smoothing angle due to the limited Cartesian resolution of the N -body simulations.

E. Theory of lensing and ISW effects

To verify our metric-reconstruction strategy, we generate and examine cosmic observables, including the lensing-convergence and (nonlinear) ISW effects.

Weak gravitational lensing by large-scale structure is due to the gravitational deflection of light by intervening matter as it travels to us. In this paper, we will focus on quantifying the weak-lensing convergence

$$\kappa \equiv \frac{D_A - \bar{D}_A}{\bar{D}_A}, \quad (33)$$

where \bar{D}_A is the unperturbed angular-diameter distance in an Friedmann Lemaître Robertson Walker (FLRW) background. Under the assumption of unperturbed photon trajectories, the so-called Born approximation, the lensing potential $\psi(r_s, \boldsymbol{\theta})$ depending on the gravitational potential ϕ for sources at comoving distance r_s (from us observers) can be defined as

$$\psi(r_s, \boldsymbol{\theta}) \equiv - \int_0^{r_s} dr' \frac{r_s - r'}{r_s r'} \times 2\Phi(r', \boldsymbol{\theta}), \quad (34)$$

and the lensing convergence is then

$$\kappa = -\frac{1}{2} \nabla^{(2)} \psi. \quad (35)$$

To avoid the need of exactly estimating the lensing potential in Eq. (34), many studies choose to introduce the radial modes and replace the angular Laplacian in Eq. (33) with the 3D Laplacian $\nabla^2 \Phi$. Then following the Newtonian Poisson equation

$$\nabla^2 \Phi = 4\pi G a^2 \bar{\rho} \delta, \quad (36)$$

Eq. (33) can be cast into an integration of the density field as

$$\kappa = \int_0^{r_s} dr' \frac{r_s - r'}{r_s r'} \times 4\pi G a^2 \bar{\rho} \delta(r', \boldsymbol{\theta}). \quad (37)$$

In practice, a more widely used scheme—the “thin-lens approximation”—relies on summing over light cone particles along lines of sight within each sky pixel. This scheme is based on Eq. (37), but it does not require radial binning or extracting the gravitational potential, and it has been employed in a number of contexts in the literature [82–86],

$$\kappa = \frac{2}{3} H_0^2 \Omega_{m,0} \frac{V_{\text{sim}}/N_{\text{sim}}}{\Omega_{\text{pix}}} \sum_{\text{particles}} \frac{1}{r_p a(r_p)} \frac{r_s - r_p}{r_s}. \quad (38)$$

Here, r_p is the comoving distance of the light cone particles and Ω_{pix} is the size of the solid angle of sky pixels. Note that even though the approximation of introducing the radial modes holds accurately on small angular scale [37], its validity is not guaranteed on largest scales.

Photons traveling through large-scale structure also encounter a time-varying potential—the ISW effect. For CMB photons, this effect alters their frequency, and hence the CMB temperature T , according to

$$\frac{\Delta T_{\text{ISW}}(r, \boldsymbol{\theta})}{T_{\text{CMB}}} = 2 \int \frac{\partial \Phi(r, \boldsymbol{\theta}, \tau)}{\partial \tau} d\tau. \quad (39)$$

One could employ Eq. (28) to estimate this ISW signal as suggested in [54]. If no knowledge of velocity fields in Eq. (28) is given, one could assume the linear growth of δ then the $\partial \Phi(r, \boldsymbol{\theta}, \tau)/\partial \tau$ field. However, the linear approach fails to capture all nonlinear effects, which soon become significant on angular scales corresponding to the multipole mode around $l \sim 60$, and will dominate the ISW contribution beyond $l \sim 100$ [54,56].

III. RESULTS

In this section, we demonstrate this new scheme’s ability to reconstruct the spacetime metric as well as the accuracy with which we can compute lensing and ISW observables. We provide a comparison of our scheme both to the output of Einstein-Boltzmann solvers (CLASS [80]) and to conventional methods found in past literature. We explore the requirements for each of these different techniques and show that for the weak-lensing and (nonlinear) ISW observables, a better than 5% accuracy for $\ell \lesssim N_{\text{side}}$ is achieved.

A. Direct potential comparison

We first evaluate the accuracy of our scheme by directly comparing the light-cone-reconstructed gravitational potential Φ with the potential obtained from snapshot data. For the first such comparison, we adopt the same configuration as in Fig. 1. The potential Φ_{snap} is computed and interpolated to HEALPix grids from a snapshot at $z = 0.3$, while the reconstructed Φ_{LC} is computed using the LC-METRIC scheme under CIC deposition, using light cone data in addition to two spatial boundary slices at $z \approx 0.03$ and $z \approx 0.52$. No snapshot information at any redshift in between is used. In Fig. 3, we calculate the angular power spectra for Φ_{snap} and Φ_{LC} . We also show their normalized cross-correlation coefficients defined as

$$r_{\ell}^{XX'} = C_{\ell}^{XX'} / \sqrt{C_{\ell}^{XX} C_{\ell}^{X'X'}} \quad (40)$$

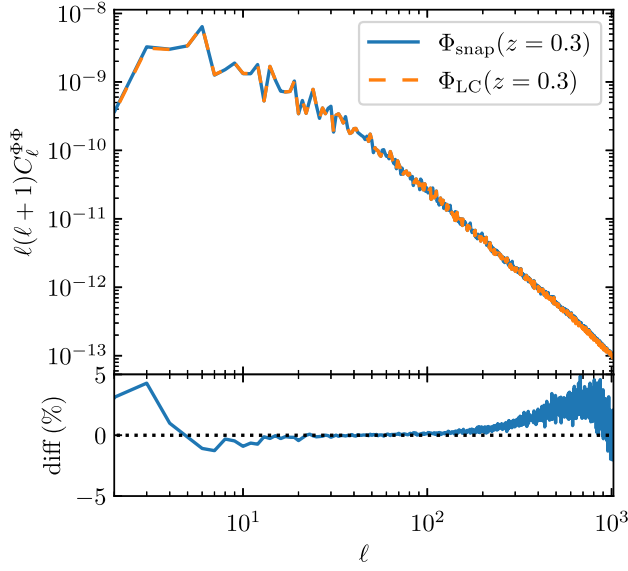


FIG. 3. Upper panel: comparison of the angular power spectrum at of Φ at $z = 0.3$ between snapshot output Φ_{snap} and the reconstructed potential Φ_{LC} from the LC-METRIC based on the light cone. Lower panel: percent difference between Φ_{snap} and Φ_{LC} . Convergence between the two methods is found as numerical resolution is increased.

in Fig. 4, where $C_\ell^{XX'}$ is the cross-power spectrum for arbitrary fields X and X' .

According to Figs. 3 and 4, highly correlated signals are in percent-level agreement for $5 \lesssim \ell \lesssim N_{\text{side}}$, with an accuracy better than 0.5% for $20 \lesssim \ell \lesssim 200$. The 5% discrepancy for $\ell \lesssim 5$, much less than the sample variance for this range of multipoles, is likely due to the approximation used by the L-PCOLA code to generate the light cone data, and to noise arising from depositing particle masses and velocities to a spherical grid. The accuracy at larger multipoles $\ell > N_{\text{side}}$ is limited by the precision of the

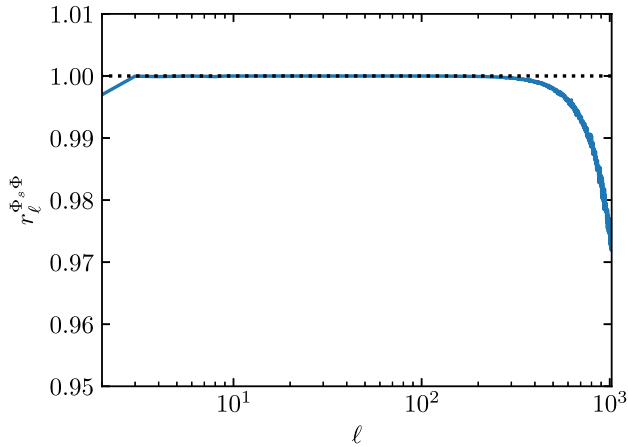


FIG. 4. Normalized cross-correlation coefficients [Eq. (40)] between the restored potential Φ_{LC} and the potential on the snapshot Φ_{snap} at $z = 0.3$.

interpolation operations (see Appendix B 2 for further discussion). The convergence test (see Appendix B 3) also suggests that we can expect an improved reliability when the angular resolution N_{side} is increased.

B. Weak lensing

The weak-lensing convergence κ can be estimated in a number of different ways for sources at the high-redshift end of the light cone ($z \approx 0.48$). The thin-lens scheme [Eq. (38)] provides one option that avoids the need to decompose the lensing (mass) distribution into radial bins at the cost of ignoring the radial modes. Another option is to compute the lensing convergence explicitly once the metric is known [Eqs. (34) and (35)] on the light cone.

We compare the probability density functions (PDF) of the lensing convergence computed using both the thin-lens approximation and explicit calculation from light-cone-reconstructed metric potential, shown in Fig. 5. The PDFs agree to 0.5% in the range of κ where the PDFs are appreciably different than zero. The reconstructed Φ_{LC} in this comparison is obtained from light cone data with the NGP mass deposition scheme in order to match the thin-lens scheme Eq. (38), which effectively employs a NGP method. Similar to the LC-METRIC scheme, the corresponding window function W_l [see Eq. (31)] is also applied to correct the power suppression after the depositing scheme is applied in the thin-lens procedure.

In addition, the lensing power spectra calculated for each of these two methods are also shown in Fig. 6, alongside a

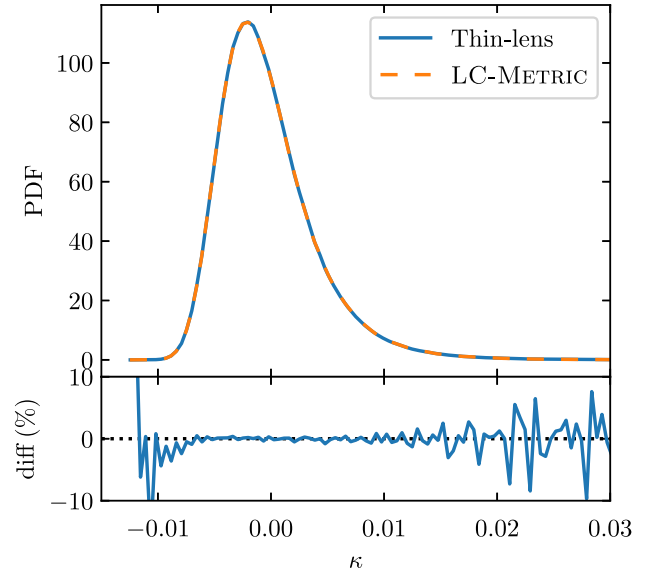


FIG. 5. Upper panel: PDFs of the lensing convergence from $z = 0.03$ – 0.48 calculated using the thin-lens approximation [Eq. (38)] and the lensing potential [Eq. (35)] based on the reconstructed metric. The mean value has been subtracted. Lower Panel: percent difference in the PDF between the thin-lens and the LC-METRIC schemes.

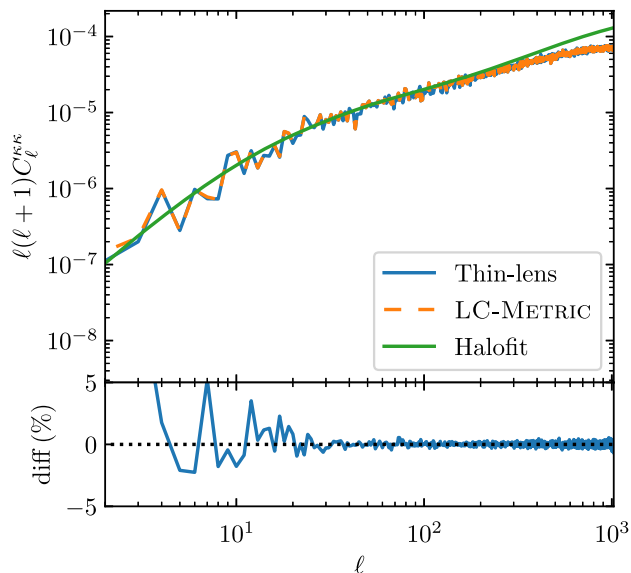


FIG. 6. Upper panel: power spectrum of the lensing convergence κ calculated with the thin-lens scheme [Eq. (38)] and the lensing potential [Eq. (35)] based on the reconstructed light cone metric Φ_{LC} from the LC-METRIC. Lower panel: percent difference between the thin-lens and the LC-METRIC schemes.

baseline power spectrum given by Halofit [87]. They are both consistent with the Halofit prediction over a wide range of scales. The discrepancy at higher ℓ is due to insufficient resolution in the N -body simulation and light cone grids, and is also observed in similar weak-lensing investigations [45,88]. Only a subpercent discrepancy is found for $\ell > 20$ between the thin lens and the LC-METRIC based scheme, suggesting the LC-METRIC reconstruction scheme is able to reproduce results that are fully consistent with the conventional thin lens approximation. The discrepancy at lower ℓ is revealing the errors of ignoring the radial modes in Eq. (37) and subsequently, Eq. (38). These radial modes turn out to have a few percent effects for the convergence at very low multipoles.

The normalized cross-correlations coefficients (Fig. 7) confirm the strong agreement between the two methods. The LC-METRIC scheme, however, can take advantage of the full metric information on the past light cone, allowing for the study of higher order effects beyond the Born approximation through a post-Born ray tracing. We leave the exploration of such effects to a future study.

C. Nonlinear ISW

The ISW effect involves the integration of the time derivative of Φ (Ξ field), which can be decomposed into $\partial_\eta + \partial_w$ in our coordinate system, see Eq. (23). However, because the power of the nonlinear ISW effect (including moving lens and Rees-Sciama effects) decays quickly at higher ℓ , high-frequency noise due to the imperfect estimation of the velocity field in this regime can easily

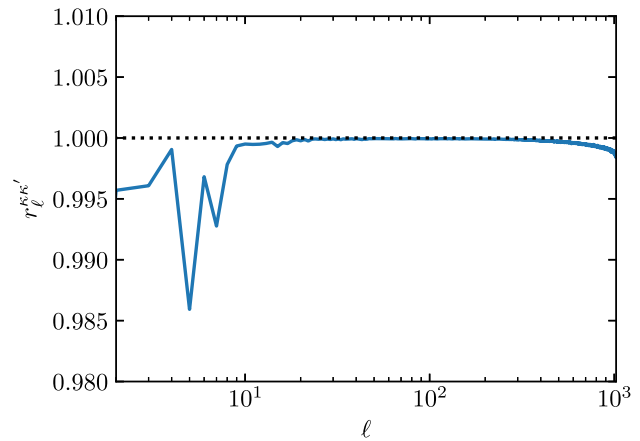


FIG. 7. Normalized cross correlation coefficients [Eq. (40)] of the lensing convergence κ between the thin-lens scheme [Eq. (38)] and the lensing potential [Eq. (35)] based on the reconstructed light cone metric Φ_{LC} .

surpass the signal. We therefore employ “thick” light cones introduced in Sec. II D, relying on the light cone data constructed from snapshots to calculate the $\partial\Phi/\partial\tau$ term using a finite differencing scheme. We truncate the $\partial\Phi/\partial\tau$ field near the boundaries (at initial and final redshift) of the light cone to avoid boundary effects. The redshift range of the ISW effect we model in this work, following the truncation, ranges from $z \approx 0.07$ – 0.47 . The snapshots used in our constructions are uniformly distributed in the space of comoving distance.

To accurately compute the ISW contributions in the highly nonlinear regime, we also implement and examine an “on-the-fly” prescription. We rerun our N -body simulations with the same parameters and a much finer time step (1024 steps). We again calculate the $\partial\Phi/\partial\tau$ using a finite differencing scheme by subtracting snapshot data on current step from the previous one. We then interpolate the $\partial\Phi/\partial\tau$ data from the Cartesian grids to our HEALPix grids, and finally, we integrate all the $\partial\Phi/\partial\tau$ data at each HEALPix pixel to evaluate the term Eq. (39). Because of the number of time steps required to ensure integration convergence (see Appendix B 5), this scheme can be taken as an accurate reference of the nonlinear ISW, though it is not an especially efficient technique for processing simulation data due to the resolution and time stepping requirements.

We have also implemented the method described in [54], which estimates $\partial\Phi/\partial\tau$ using Eq. (28) on every output snapshot. After obtaining all the $\partial\Phi/\partial\tau$ data, similar to [54], we perform 1024 interpolations between snapshots and finally integrate these to estimate Eq. (39).

Comparisons of the ISW power spectrum calculated using these different schemes are shown in Fig. 8. All of the schemes show agreement with the linear ISW power spectrum at low ℓ and begin to deviate from the linear result at $\ell > 60$, consistent with previous studies

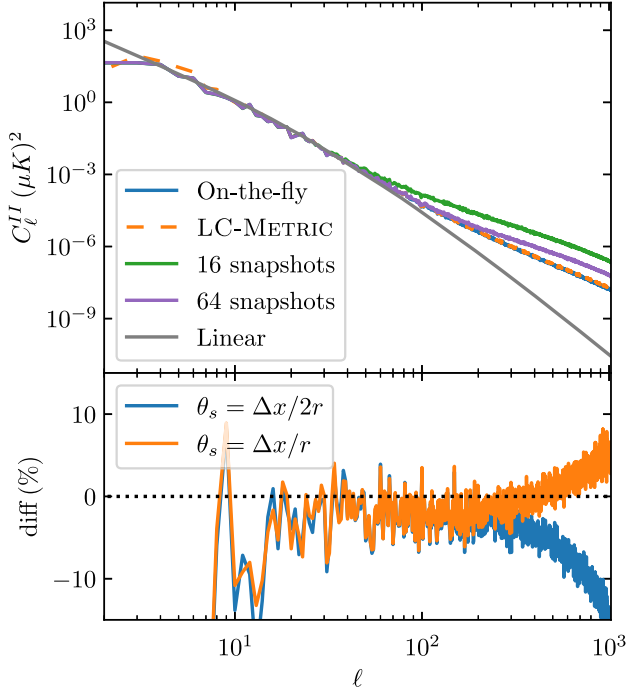


FIG. 8. Upper panel: power spectrum of the ISW field calculated by integrating snapshots from Eq. (28) and the reconstructed “thick” light cones scheme using LC-METRIC based on 16 snapshots with smoothing angle $\theta_s = \Delta x/2r$. Lower panel: percent difference between on-the-fly reference and “thick” light cones LC-METRIC scheme with different smoothing angles θ_s .

[54,56,59]. The interpolation scheme based on 16 snapshots significantly overestimates the power compared to the on-the-fly reference spectrum. Increasing the number of snapshots to 64 improves the accuracy but still gives an order of magnitude overestimation. Even though the “thick” light cones scheme shown here is based on the light cone constructed from only 16 snapshots, it coincides with the reference spectrum with an accuracy better than 5% for $\ell < N_{\text{side}}$. We also note that at the nonlinear scale, the ISW spectra highly depends on the manually applied smoothing scale we used as in Eq. (32), whereas the on-the-fly reference scheme includes an intrinsic smoothing scale, whose correspondence to the angular smoothing scale in the LC-METRIC is unknown. Instead of looking for the manually applied smoothing angle that best fits the reference on-the-fly scheme, we look for the range of smoothing scale which gives good estimation to the ISW power to the highly nonlinear scale. In the lower panel in Fig. 8, we show the ratio between the on-the-fly reference and the LC-METRIC scheme under two different angular smoothing scales: $\theta_s = \Delta x/r$ and $\theta_s = \Delta x/2r$, where the later one with a smaller angle naturally produces higher power. Within this range of smoothing scale, an accuracy better than 5% for $\ell < N_{\text{side}}$ and 15% for $\ell < 2N_{\text{side}}$ can be achieved. On the other hand, as shown in Fig. 9, the normalized cross correlation between the LC-METRIC

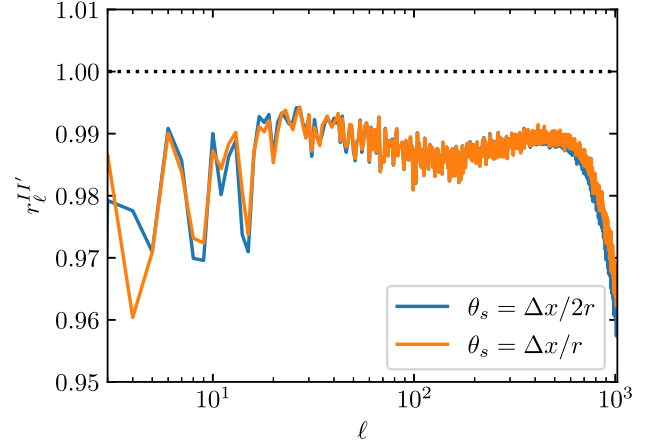


FIG. 9. Normalized cross correlation coefficients [Eq. (40)] of the ISW fields between the on-the-fly scheme based on Eq. (28) and the reconstructing “thick” light cones scheme based on LC-METRIC with different smoothing angle θ_s .

scheme and the on-on-fly scheme is almost independent of the smoothing scale. The minor power suppression (lower panel in Fig. 8) and lack of correlation is again due to the insufficient angular resolution and also the systematics in our construction scheme of light cones from snapshots. See Appendices B 5 and C for more details on the light cone construction scheme.

IV. SUMMARY

In this work, we have presented a novel scheme LC-METRIC, which is able to quantify cosmic observables by postprocessing simulated large-scale structure data. This reconstruction procedure is based on obtaining solutions to the linearized Einstein’s equations on light cone grids with a relaxation scheme; it is also a flexible scheme that is able to process ordinary snapshots or light cone outputs.

We have also generated mock cosmic observables including the weak-lensing convergence field and the (nonlinear) ISW effect based on the reconstructed metric potential provided by LC-METRIC. For the weak-lensing calculation, under the Born approximation, the lensing power spectrum calculated explicitly from the reconstructed metric agrees, typically at a subpercent level, with the equivalent spectrum calculated via the traditional thin-lens approach, although percent-level disagreement is found on large scales. Both results are in general agreement with the prediction given by the Halofit prescription over a wide range of scales. For the estimation of the ISW and Rees-Sciama effects, as a postprocessing method, the LC-METRIC-based “thick” light cone scheme is able to model the ISW signal in a highly nonlinear regime and maintain a better than 5% precision for $\ell < N_{\text{side}}$ with a proper smoothing angle when compared to a high-precision reference on-the-fly calculation. When compared to other postprocessing schemes such as the one introduced in [54],

LC-METRIC is able to provide a much more precise prediction of nonlinear ISW contributions, which include the Rees-Sciama and moving-lens effects, based on data from considerably fewer N -body simulation snapshots. Since weak-lensing observables mostly depend on the angular gradient (Laplacian) of the gravitational fields, whereas the ISW effect depends on the time (radial) gradient, being able to predict these two effects precisely demonstrates the utility of the LC-METRIC prescription. Therefore, we conclude that LC-METRIC is able to reconstruct the metric accurately in both linear and highly nonlinear regimes, and hence it is suitable for simulating data relevant to current and future large-scale surveys.

There are still several improvements that could be made to the LC-METRIC in the future. First, even though our current implementation for the LC-METRIC only supports running on a shared memory node, the algorithm can be easily implemented to support distributed memory, which will relieve the relatively stringent memory requirements [currently $\mathcal{O}(N \log N)$, where N is the number of spherical grids]. Second, the overall accuracy of the fields, especially the accuracy of Ξ term in Eq. (23), can be potentially improved by a more accurate deposition technique of the radial velocity field, e.g. Delaunay tessellation field interpolation [89,90]. Finally, a general-relativistic ray-tracing component has been implemented, which is necessary in order to quantify higher-order and post-Born effects. We will investigate those effects in a future study.

Upcoming large-area and high-precision galaxy and CMB surveys will deepen our understanding of the Universe as well as bring unprecedented challenges for modeling general-relativistic cosmic observables such as weak-lensing, the Rees-Sciama effect, moving-lens effect, kSZ effect, etc. The LC-METRIC scheme provides a universal way to model these effects while maintaining a high level of precision even in the highly nonlinear regime, making it well-suited to testing and analyzing catalogs for these surveys in the future. Knowledge of the spacetime metric will also facilitate the estimation of other relativistic or light cone projections effects that have not been properly quantified and measured, as listed in [33]. Furthermore, the postprocessing-based feature of LC-METRIC will allow for consistent analysis of N -body simulations or emulations running with different physics. We expect that this new scheme will provide us with some insight into reconstructing metric information from observations while simultaneously accounting for different relativistic and projection effects. The reconstructed cosmic density and velocity fields are needed for such reconstruction; while the former may be estimated from galaxy or halo catalogs [91,92], the later may be restored from e.g. kinetic Sunyaev Zeldovich (kSZ) [93] or observations of the moving lens effect.

Finally, we note a recent study [94] that points out the value of determining the “boosted potential” in order to

improve our understanding of several aspects of structure formation. This scheme relies on quantifying the gravitational potential in a boosted frame. Our new approach for constructing the gravitational potential on the light cone is suitable for extracting the boosted potential based on light cone data. We reserve further investigation in this direction for future work.

To summarize, we have introduced the LC-METRIC scheme for constructing the spacetime metric from general N -body-code outputs. We have demonstrated its accuracy by comparing it to conventional methods in quantifying the weak-lensing convergence and the nonlinear-ISW effects. Therefore, it is possible to incorporate LC-METRIC with general N -body catalogs and facilitate estimation of higher-order and post-Born relativistic effects on cosmological observables.

ACKNOWLEDGMENTS

We thank Stefano Anselmi and Selim Hotinli for useful discussions and feedback. J. B. M. is partly supported by a Department of Energy Grant No. DE-SC0017987 to the particle astrophysics theory group at WUSTL. G. D. S. is partly supported by a Department of Energy Grant No. DE-SC0009946 to the particle astrophysics theory group at CWRU. The simulations and analyses in this work used the Data Storage Platform and Scientific Compute Platform operated by the Research Infrastructure Services (RIS) of Washington University in St. Louis.

APPENDIX A: SOLVING THE HYPERBOLIC FORM OF THE LINEARIZED EINSTEIN EQUATIONS

1. Derivations

In this appendix, we show in detail how to derive the hyperbolic form of the linearized Einstein equations [Eqs. (22) and (23)].

With the shorthands introduced in Eq. (24), by combing the coordinate transformations in Eqs. (18) to (21) for pressureless fluid, Eq. (10) in the linearized Einstein equations can be written as

$$\Phi'' + 2\dot{\Phi}' + \ddot{\Phi} + 3\mathcal{H}(\dot{\Phi} + \Phi') + (2\dot{\mathcal{H}} + \mathcal{H}^2)\Phi = 0, \quad (\text{A1})$$

and Eq. (9) can be rewritten as

$$\Phi'' + \dot{\Phi}' + \mathcal{H}\Phi' = -4\pi G a^2 v_r. \quad (\text{A2})$$

We combine Eqs. (A1) and (A2) to remove the Φ'' term, obtaining

$$\begin{aligned} \dot{\Phi}' &= -2\dot{\Phi}' + \ddot{\Phi} + 3\mathcal{H}(\dot{\Phi} + \Phi') \\ &+ (2\dot{\mathcal{H}} + \mathcal{H}^2)\Phi - \mathcal{H}\Phi' + 4\pi G a^2 \bar{\rho} v_r. \end{aligned} \quad (\text{A3})$$

The Laplacian operator applied to Φ can also be written as

$$\nabla^2\Phi \equiv \frac{1}{r}(2\Phi' + r\Phi'') + \nabla^{(2)}\Phi/r^2, \quad (\text{A4})$$

where $\nabla^{(2)}\Phi \equiv \frac{1}{\sin\theta}(\sin\theta\frac{\partial\Phi}{\partial\theta}) + \frac{1}{\sin^2\theta}\frac{\partial^2\Phi}{\partial^2\phi}$. By combining Eqs. (A1), (A4), and (8), and again removing the Φ'' term, we find that

$$\ddot{\Phi} = \frac{2}{r}\dot{\Phi}' - 2\dot{\Phi}' - 6\mathcal{H}\dot{\Phi} - 6\mathcal{H}\Phi' - (2\dot{\mathcal{H}} + 4\mathcal{H}^2)\Phi - 4\pi Ga^2\bar{\rho}\delta + \frac{\nabla^{(2)}\Phi}{r^2}. \quad (\text{A5})$$

Considering the redefinition of the variables Eq. (25), and the relativistic corrections to the density contrast Eqs. (15), (A5), and (A3) can be cast into Eqs. (22) and (23).

2. Discretization scheme and multigrid solver

We discretized all variables in Eqs. (22) and (23) with multiple HEALPix maps at discretized comoving

distances. For example, the gravitational potential Φ is discretized as $\Phi(r_j, \theta_{\text{pix}})$, where j is the radial index and θ_{pix} is a HEALPix pixel. The radial sampling points are chosen so that the comoving radial direction of the light cone is evenly sampled with a constant spacing Δr .

With this discretization scheme, once the boundary data represented by two HEALPix maps at the smallest and the largest comoving radius, r_i and r_f , are given, Eqs. (22) and (23) becomes a 1D boundary value problem. Newtonian relaxation, boosted by a multigrid method, is employed to solve this problem. The initial guess for the relaxation scheme is provided by trivially linearly interpolating all the radial grids between the boundary conditions at r_i and r_f .

The relaxation is performed on the gravitational potential Φ in Eq. (22), with a second-order finite-difference scheme: at relaxation step s and grid index j (omitting the θ dependence), Φ , Π , and Ξ have the old values Φ_j^{old} , Π_j^{old} , and Ξ_j^{old} . The new value for Φ_j after one iteration step is

$$\Phi_j^{\text{new}} = \frac{(-2/r + 2\mathcal{H})\Pi_j^{\text{old}} + 4\pi Ga^2\bar{\rho}_j(\delta_j + 2v_{r,j}) - (\Phi_{j+1}^{\text{old}} + \Phi_{j-1}^{\text{old}})/\Delta r^2}{-2/\Delta r^2 + \nabla^{(2)}/r^2 + 2(\dot{\mathcal{H}} - \mathcal{H}^2 - 4\pi Ga^2\bar{\rho}_j)}, \quad (\text{A6})$$

where $\nabla^{(2)}$ can be simply replaced by $\ell(\ell+1)$ when solving this equation in the spherical harmonic basis. During the relaxation, the Ξ field, defined as $\Xi \equiv \dot{\Phi} + \Phi'$ in Eq. (23), is solved by a second-order Runge-Kutta scheme, which means the value of Ξ will be updated at every iteration. By definition [Eq. (25)], the Π field can also be calculated from the Ξ field.

The multigrid method is a widely used method to accelerate the convergence rate of a standard relaxation scheme by constructing a hierarchy of grids where levels in the hierarchy from top to bottom have resolutions ranging from coarsest to finest. One is seeking for the solution on the finest grids.

The essence of the multigrid method is that instead of performing a large number of relaxations on the finest level until it converges, it performs only several relaxations on each level, then “restricts” the current solution and errors to a coarser grid and solve the residual equations on the coarser level where the corrections to the resolutions on finer level are calculated through another several relaxations. Finally, those corrections at the coarser level are “prolonged” to the finer level to correct the current approximate solution and significantly speed-up the convergence rate. We refer to [95,96] for more details about the multigrid method.

Performing the above procedure recursively from the finest to coarsest level, and back to the finest level is called

a V-cycle. In this study, we build a multigrid hierarchy with five levels and repeatedly perform V-cycles until the desired precision is achieved.

APPENDIX B: NUMERICAL VALIDATION

In this appendix, we will show several convergence tests we have performed to validate our results.

1. Convergence of the multigrid solver

We estimate the convergence of our LC-METRIC solver from the L2 norm of the relative error $\|E\|/\|\ddot{\Phi}\|$ and show the result in Fig. 10, where E is the error of Eq. (22) and $\|\ddot{\Phi}\|$ represents the L2 norm of its left-hand side. The radial and angular resolution of the light cone grids are $N_\eta = 1024$ and $N_{\text{side}} = 512$, respectively, and the number of levels of the multigrid hierarchy is five. Our multigrid scheme will reduce the relative error very efficiently until reaching a plateau. The final plateau in Fig. 10 is limited by the machine precision of 32-bit float used in the solver. The total memory consumption is about 10 times the memory consumption of the light cone grids, and the time consumption for 100 iterations is about 20 hours on a computer node with 28 CPUs.

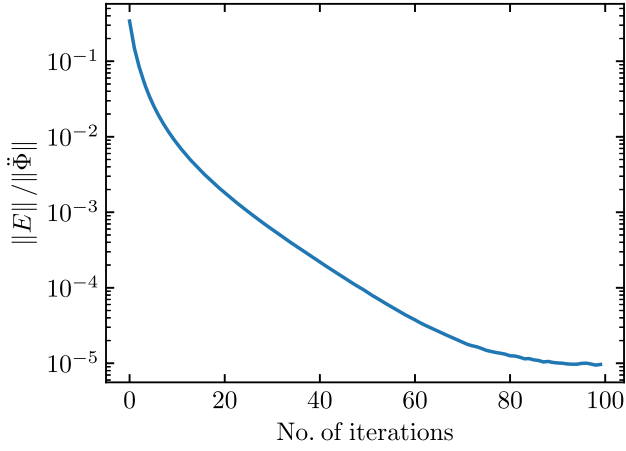


FIG. 10. Evolution of L2 norm of relative error of Eq. (22) with respect to the number of V-cycles performed.

2. Numerical convergence of the interpolations to HEALPix grids

When calculating a reference power spectrum of the gravitational potential or ISW (see Secs. III A and III C), or when setting initial conditions for the solver, interpolations of fields from Cartesian grids to HEALPix grids are performed. We test the accuracy of such operations by linearly interpolating the same potential fields on Cartesian grids with different angular resolutions. As shown in Fig. 11, by comparing the ratio of angular power between different N_{side} s, we can estimate the accuracy of such interpolations from Cartesian grids to HEALPix grids, which is better than 5% for $\ell < N_{\text{side}}$, and better than 20% for $\ell < 2N_{\text{side}}$. This limits the numerical precision of both reference power spectra and the LC-METRIC scheme.

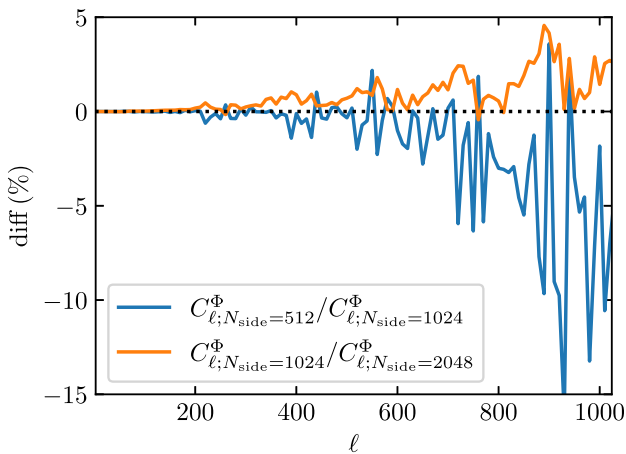


FIG. 11. The ratio of the angular power spectrum of Φ interpolated from Cartesian grids with different HEALPix resolutions N_{side} . The radius for such interpolations is set according to $r = \sqrt{(A/\Omega)}$, where A is the Cartesian resolution square dx^2 and Ω is the HEALPix solid angle for $N_{\text{side}} = 512$.

3. Numerical convergence of the gravitational potential

Even though the precision of power spectra at higher ℓ is primarily limited by linear interpolation accuracy as described in the previous subsection, as suggested by Fig. 12, improving the angular resolution N_{side} can potentially improve the precision at higher ℓ , since the cross correlation at the same ℓ is significantly larger when comparing the result of $N_{\text{side}} = 512$ with $N_{\text{side}} = 256$.

4. Numerical convergence of weak lensing

The weak-lensing observables extracted from reconstructed metric from light cone data are independent of the radial resolution chosen for our coordinate system. The test of the convergence against different radial resolutions is shown in Fig. 13. No noticeable differences are identified for reasonable resolutions from 256 to 1024, suggesting the

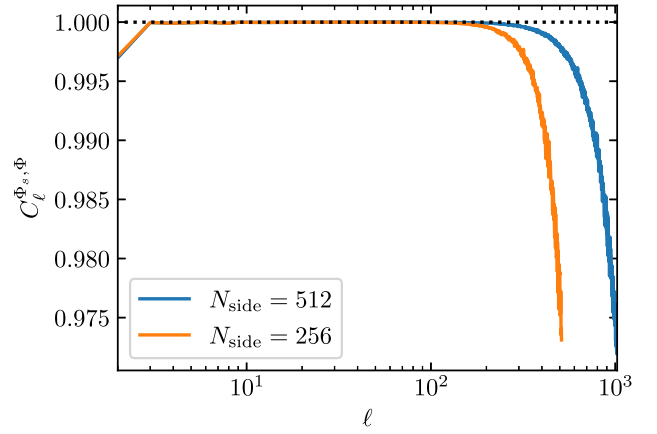


FIG. 12. The same as Fig. 4. Normalized cross correlation coefficients between the reconstructed Φ_{LC} and the Φ_{snap} under different N_{side} .

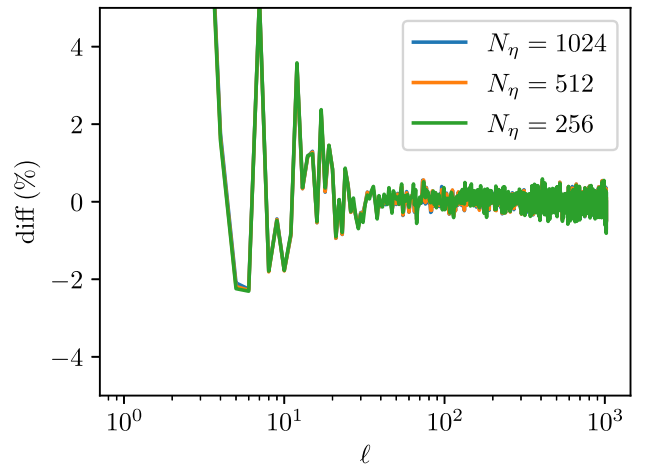


FIG. 13. Ratio of the thin-lens approach to the scheme based on the LC-METRIC reconstruction with different radial resolution N_{η} , same as lower panel in Fig. 6.

robustness of the numerical value of weak-lensing convergence calculated by the LC-METRIC scheme.

5. Numerical convergence of the ISW and Rees-Sciama effects

The reference ISW power spectrum calculated through the on-the-fly scheme in Fig. 8 is extracted from a N -body simulation performing $N_{\text{steps}} = 1024$ time steps. Figure 14 validates this choice of number of time steps by comparing the ISW power with different number of time steps since the results of $N_{\text{steps}} = 512$ and $N_{\text{steps}} = 1024$ overlap. We also calculate the convergence rate R_{conv} , defined as

$$R_{\text{conv}} = \frac{|f_{N_m} - f_{N_c}|}{|f_{N_c} - f_{N_f}|}, \quad (\text{B1})$$

where $f_{N_c}, f_{N_m}, f_{N_f}$ are values calculated at resolutions N_c, N_m, N_f , which are from coarsest to finest, and shown in the lower panel in Fig. 14 that the rate is beyond the linear convergence for the $\ell > 200$ region.

The minor lack of correlation between the reference ISW power and the reconstructed one through “thick” light cones (Fig. 9) is likely due to the systematic bias when creating light cone data from snapshots (see Appendix C for more detail). This can be confirmed by comparing the blue and green curve in Fig. 15, where employing more snapshots to construct “thick” light cones will improve the correlation. The suppression of power at higher ℓ is again due to the limited precision of the linear interpolations,

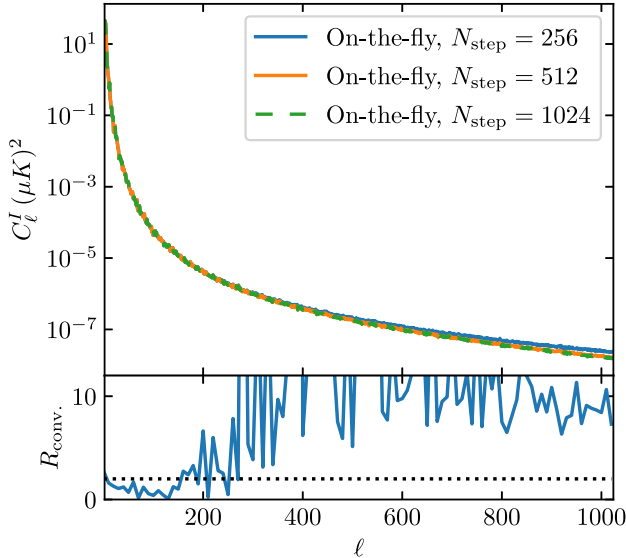


FIG. 14. Upper panel: ISW and Rees-Sciama effects calculated through on-the-fly method against number of time steps. Convergent result is achieved when $N_{\text{steps}} = 1024$. Lower panel: convergence rate R_{conv} , defined in Eq. (B1), the result is higher than the linear convergence rate (dotted line) for $\ell > 200$.

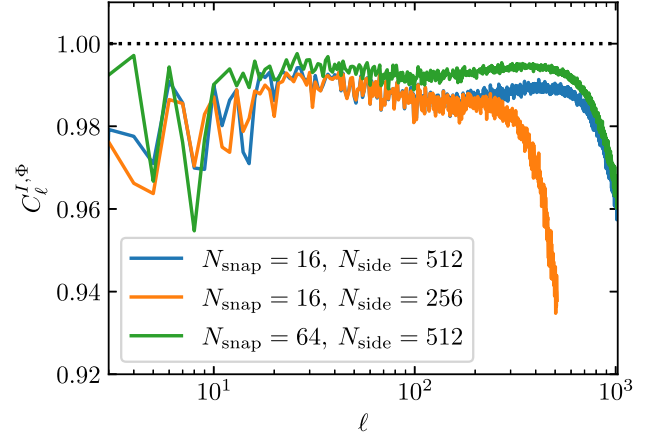


FIG. 15. Same as Fig. 9. Variations of normalized cross correlation coefficients of the ISW fields between the snapshots scheme and the reconstructing “thick” light cones against different numbers of snapshots and different angular resolutions N_{side} .

which can be improved by employing a higher angular resolution according to Fig. 15.

APPENDIX C: LIGHT CONE CONSTRUCTION FROM SNAPSHOTS

The scheme integrated in the LC-METRIC to construct light cone data from snapshots is similar to the particle extrapolations scheme mentioned in [97]. Several improvements have been implemented to enhance the construction accuracy. Here, we will give our full algorithm on constructing light cones from snapshots.

For each particle inside the light cone, which has comoving position \mathbf{r}_i , peculiar velocity \mathbf{v}_i , and acceleration \mathbf{a}_i on the snapshot at conformal time τ_i , the time it crosses the light cone is $\tau + \delta\tau$, and the corresponding comoving radii after the time $\delta\tau$ is

$$\begin{aligned} |\mathbf{r}| &= \left| \mathbf{r}_i + \mathbf{v}_i \delta\tau + \frac{\mathbf{a}_i}{2} \tau^2 \right|, \\ &\approx |\mathbf{r}_i| + \delta\tau \frac{\mathbf{r}_i \cdot \mathbf{v}_i}{|\mathbf{r}_i|} \\ &\quad - \delta\tau^2 \left[\frac{(\mathbf{r}_i \cdot \mathbf{v}_i)^2}{2|\mathbf{r}_i|^3} + \frac{\mathbf{v}_i \cdot \mathbf{v}_i}{2|\mathbf{r}_i|} + \frac{\mathbf{a}_i \cdot \mathbf{r}_i}{2|\mathbf{r}_i|} \right], \end{aligned} \quad (\text{C1})$$

note we have kept up to second-order terms, and the acceleration \mathbf{a}_i can be estimated from difference between peculiar velocities between two adjacent snapshots from

$$\mathbf{a}_i = (\mathbf{v}_{i+1} - \mathbf{v}_i) / \Delta\tau, \quad (\text{C2})$$

where $\Delta\tau$ is the difference in the conformal time τ between these two snapshots. Additionally, since the background light cone satisfies $\tau = -|\mathbf{r}|$, we can write down the following relation

$$|r| = \tau_i - \delta\tau. \quad (\text{C3})$$

After plugging in Eq. (C1) to Eq. (C3), we can solve $\delta\tau$ from the quadratic equation. However, the following optimizations are necessary to construct the light cone accurately:

- (i) For particle p_j outside the light cone on a snapshot s_i , we do not extrapolate this particle since it will never enter the light cone in the future.
- (ii) For particle p_j inside the light cone on a snapshot s_i , if p_j inside the next snapshot (snapshot s_{j+1}) is still inside the light cone, we do not extrapolate this particle.
- (iii) We use the second-order quadratic approximation to solve Eq. (C1) instead of the exact solution to avoid possible numerical instabilities.
- (iv) If the solution of $\delta\tau$ satisfies $\delta\tau > \Delta\tau$, no extrapolation will be performed.

Note that this scheme will tend to omit some particles crossing the light cone because of the limited accuracy of the quadratic interpolation, and therefore it will introduce some systematic bias to the reconstructed light cone. Investigating an improved scheme to reduce this bias is left for future study.

-
- [1] M. Schmittfull and U. Seljak, *Phys. Rev. D* **97**, 123540 (2018).
 - [2] A.-S. Deutsch, E. Dimastrogiovanni, M. Fasiello, M. C. Johnson, and M. Münchmeyer, *Phys. Rev. D* **100**, 083538 (2019).
 - [3] M. Münchmeyer, M. S. Madhavacheril, S. Ferraro, M. C. Johnson, and K. M. Smith, *Phys. Rev. D* **100**, 083508 (2019).
 - [4] J. I. Cayuso and M. C. Johnson, *Phys. Rev. D* **101**, 123508 (2020).
 - [5] S. C. Hotinli, J. B. Mertens, M. C. Johnson, and M. Kamionkowski, *Phys. Rev. D* **100**, 103528 (2019).
 - [6] P.-S. Corasaniti, T. Giannantonio, and A. Melchiorri, *Phys. Rev. D* **71**, 123521 (2005).
 - [7] S. Nakamura, A. De Felice, R. Kase, and S. Tsujikawa, *Phys. Rev. D* **99**, 063533 (2019).
 - [8] K. Ichikawa and T. Takahashi, *J. Cosmol. Astropart. Phys.* **02** (2008) 017.
 - [9] A. Torres-Rodriguez and C. M. Cress, *Mon. Not. R. Astron. Soc.* **376**, 1831 (2007).
 - [10] Y. Akrami, R. Kallosh, A. Linde, and V. Vardanyan, *J. Cosmol. Astropart. Phys.* **06** (2018) 041.
 - [11] Z. Pan and M. C. Johnson, *Phys. Rev. D* **100**, 083522 (2019).
 - [12] D. Contreras, M. C. Johnson, and J. B. Mertens, *J. Cosmol. Astropart. Phys.* **10** (2019) 024.
 - [13] S. C. Hotinli, M. C. Johnson, and J. Meyers, *Phys. Rev. D* **103**, 043536 (2021).
 - [14] P. A. Abell *et al.* (LSST Science, LSST Project Collaborations), [arXiv:0912.0201](https://arxiv.org/abs/0912.0201).
 - [15] C. S. Lorenz, D. Alonso, and P. G. Ferreira, *Phys. Rev. D* **97**, 023537 (2018).
 - [16] S. Tassev, M. Zaldarriaga, and D. Eisenstein, *J. Cosmol. Astropart. Phys.* **06** (2013) 036.
 - [17] C. Howlett, M. Manera, and W. J. Percival, *Astron. Comput.* **12**, 109 (2015).
 - [18] A. Izard, M. Crocce, and P. Fosalba, *Mon. Not. R. Astron. Soc.* **459**, 2327 (2016).
 - [19] Y. Feng, M.-Y. Chu, U. Seljak, and P. McDonald, *Mon. Not. R. Astron. Soc.* **463**, 2273 (2016).
 - [20] G. Stein, M. A. Alvarez, and J. R. Bond, *Mon. Not. R. Astron. Soc.* **483**, 2236 (2019).
 - [21] M. Colavincenzo *et al.*, *Mon. Not. R. Astron. Soc.* **482**, 4883 (2019).
 - [22] M. Borzyszkowski, D. Bertacca, and C. Porciani, *Mon. Not. R. Astron. Soc.* **471**, 3899 (2017).
 - [23] M. Jalilvand, B. Ghosh, E. Majerotto, B. Bose, R. Durrer, and M. Kunz, *Phys. Rev. D* **101**, 043530 (2020).
 - [24] W. L. Matthewson and R. Durrer, [arXiv:2107.00467](https://arxiv.org/abs/2107.00467).
 - [25] A. Petri, Z. Haiman, and M. May, *Phys. Rev. D* **95**, 123503 (2017).
 - [26] E. Krause and C. M. Hirata, *Astron. Astrophys.* **523**, A28 (2010).
 - [27] D. Munshi, T. Namikawa, T. D. Kitching, J. D. McEwen, R. Takahashi, F. R. Bouchet, A. Taruya, and B. Bose, *Mon. Not. R. Astron. Soc.* **493**, 3985 (2020).
 - [28] B. M. Schaefer, L. Heisenberg, A. F. Kalovidouris, and D. J. Bacon, *Mon. Not. R. Astron. Soc.* **420**, 455 (2012).
 - [29] H. L. Bester, J. Larena, P. J. van der Walt, and N. T. Bishop, *J. Cosmol. Astropart. Phys.* **02** (2014) 009.
 - [30] H. L. Bester, J. Larena, and N. T. Bishop, in *14th Marcel Grossmann Meeting on Recent Developments in Theoretical and Experimental General Relativity, Astrophysics, and Relativistic Field Theories* (World Scientific Publishing Company, 2017), Vol. 3, pp. 2284–2289.
 - [31] M. R. Becker, [arXiv:1210.3069](https://arxiv.org/abs/1210.3069).
 - [32] A. Challinor and A. Lewis, *Phys. Rev. D* **84**, 043516 (2011).
 - [33] C. Bonvin and R. Durrer, *Phys. Rev. D* **84**, 063505 (2011).
 - [34] S. C. Hotinli, J. Meyers, N. Dalal, A. H. Jaffe, M. C. Johnson, J. B. Mertens, M. Münchmeyer, K. M. Smith, and A. van Engelen, *Phys. Rev. Lett.* **123**, 061301 (2019).
 - [35] Y.-C. Cai, S. Cole, A. Jenkins, and C. S. Frenk, *Mon. Not. R. Astron. Soc.* **407**, 201 (2010).
 - [36] K. Kainulainen and V. Marra, *Phys. Rev. D* **84**, 063004 (2011).
 - [37] B. Jain, U. Seljak, and S. D. M. White, *Astrophys. J.* **530**, 547 (2000).
 - [38] T. Hamana and Y. Mellier, *Mon. Not. R. Astron. Soc.* **327**, 169 (2001).
 - [39] S. Hilbert, J. Hartlap, S. D. M. White, and P. Schneider, *Astron. Astrophys.* **499**, 31 (2009).
 - [40] J. Harnois-Deraps, S. Vafaei, and L. Van Waerbeke, *Mon. Not. R. Astron. Soc.* **426**, 1262 (2012).

- [41] M. Petkova, R. B. Metcalf, and C. Giocoli, *Mon. Not. R. Astron. Soc.* **445**, 1954 (2014).
- [42] P. Fosalba, E. Gaztanaga, F. Castander, and M. Manera, *Mon. Not. R. Astron. Soc.* **391**, 435 (2008).
- [43] G. Fabbian, M. Calabrese, and C. Carbone, *J. Cosmol. Astropart. Phys.* **02** (2018) 050.
- [44] C. Gouin, R. Gavazzi, C. Pichon, Y. Dubois, C. Laigle, N. E. Chisari, S. Codis, J. Devriendt, and S. Peirani, *Astron. Astrophys.* **626**, A72 (2019).
- [45] F. Lepori, J. Adamek, R. Durrer, C. Clarkson, and L. Coates, *Mon. Not. R. Astron. Soc.* **497**, 2078 (2020).
- [46] J. T. Giblin, J. B. Mertens, G. D. Starkman, and A. R. Zentner, *Phys. Rev. D* **96**, 103530 (2017).
- [47] J. Wambsganss, R. Cen, and J. P. Ostriker, [arXiv:astro-ph/9610096](https://arxiv.org/abs/astro-ph/9610096).
- [48] A. Petri, *Astron. Comput.* **17**, 73 (2016).
- [49] S. Das and P. Bode, *Astrophys. J.* **682**, 1 (2008).
- [50] S. Hilbert *et al.*, *Mon. Not. R. Astron. Soc.* **493**, 305 (2020).
- [51] G. Marozzi, G. Fanizza, E. Di Dio, and R. Durrer, *Phys. Rev. Lett.* **118**, 211301 (2017).
- [52] G. Marozzi, G. Fanizza, E. Di Dio, and R. Durrer, *Phys. Rev. D* **98**, 023535 (2018).
- [53] G. Marozzi, G. Fanizza, E. Di Dio, and R. Durrer, *J. Cosmol. Astropart. Phys.* **09** (2016) 028.
- [54] Y.-C. Cai, S. Cole, A. Jenkins, and C. S. Frenk, *Mon. Not. R. Astron. Soc.* **407**, 201 (2010).
- [55] C. Carbone, M. Petkova, and K. Dolag, *J. Cosmol. Astropart. Phys.* **07** (2016) 034.
- [56] J. Adamek, Y. Rasera, P. S. Corasaniti, and J.-M. Alimi, *Phys. Rev. D* **101**, 023512 (2020).
- [57] W. A. Watson *et al.*, *Mon. Not. R. Astron. Soc.* **438**, 412 (2014).
- [58] K. Naidoo, P. Fosalba, L. Whiteway, and O. Lahav, *Mon. Not. R. Astron. Soc.* **506**, 4344 (2021).
- [59] F. Hassani, J. Adamek, and M. Kunz, *Mon. Not. R. Astron. Soc.* **500**, 4514 (2020).
- [60] V. Springel, *Mon. Not. R. Astron. Soc.* **364**, 1105 (2005).
- [61] M. J. Fullana, J. V. Arnaud, R. J. Thacker, H. M. P. Couchman, and D. Sáez, *Mon. Not. R. Astron. Soc.* **464**, 3784 (2017).
- [62] G. Pratten and A. Lewis, *J. Cosmol. Astropart. Phys.* **08** (2016) 047.
- [63] <https://github.com/ctian282/lcmetric>.
- [64] S. Weinberg, *Cosmology* (Oxford University Press, Oxford, 2008).
- [65] J. Adamek, D. Daverio, R. Durrer, and M. Kunz, *J. Cosmol. Astropart. Phys.* **07** (2016) 053.
- [66] J. T. Giblin, J. B. Mertens, G. D. Starkman, and C. Tian, *Phys. Rev. D* **99**, 023527 (2019).
- [67] C. Barrera-Hinojosa and B. Li, *J. Cosmol. Astropart. Phys.* **01** (2020) 007.
- [68] E. Bentivegna and M. Bruni, *Phys. Rev. Lett.* **116**, 251302 (2016).
- [69] H. J. Macpherson, D. J. Price, and P. D. Lasky, *Phys. Rev. D* **99**, 063522 (2019).
- [70] W. E. East, R. Wojtak, and F. Pretorius, *Phys. Rev. D* **100**, 103533 (2019).
- [71] J. Adamek, C. Clarkson, D. Daverio, R. Durrer, and M. Kunz, *Classical Quantum Gravity* **36**, 014001 (2019).
- [72] N. E. Chisari and M. Zaldarriaga, *Phys. Rev. D* **83**, 123505 (2011); **84**, 089901(E) (2011).
- [73] G. Ellis, S. Nel, R. Maartens, W. Stoeger, and A. Whitman, *Phys. Rep.* **124**, 315 (1985).
- [74] M. Gasperini, G. Marozzi, F. Nugier, and G. Veneziano, *J. Cosmol. Astropart. Phys.* **07** (2011) 008.
- [75] G. Fanizza, G. Marozzi, M. Medeiros, and G. Schiaffino, *J. Cosmol. Astropart. Phys.* **02** (2021) 014.
- [76] When solving Eq. (23), we only need to impose a boundary condition at high redshift.
- [77] R. Fedorenko, *USSR Computational Mathematics and Mathematical Physics* **1**, 1092 (1962).
- [78] C. Howlett, M. Manera, and W. J. Percival, *Astron. Comput.* **12**, 109 (2015).
- [79] S. Tassev, M. Zaldarriaga, and D. Eisenstein, *J. Cosmol. Astropart. Phys.* **06** (2013) 036.
- [80] D. Blas, J. Lesgourgues, and T. Tram, *J. Cosmol. Astropart. Phys.* **07** (2011) 034.
- [81] R. W. Hockney and J. W. Eastwood, *Computer Simulation Using Particles* (CRC Press, Boca Raton, 1981).
- [82] R. Teyssier, S. Pires, S. Prunet, D. Aubert, C. Pichon, A. Amara, K. Benabed, S. Colombi, A. Refregier, and J.-L. Starck, *Astron. Astrophys.* **497**, 335 (2009).
- [83] A. Kiessling, A. F. Heavens, and A. N. Taylor, *Mon. Not. R. Astron. Soc.* **414**, 2235 (2011).
- [84] J. I. Cayuso, M. C. Johnson, and J. B. Mertens, *Phys. Rev. D* **98**, 063502 (2018).
- [85] R. Takahashi, T. Hamana, M. Shirasaki, T. Namikawa, T. Nishimichi, K. Osato, and K. Shiroyama, *Astrophys. J.* **850**, 24 (2017).
- [86] A. Izard, P. Fosalba, and M. Crocce, *Mon. Not. R. Astron. Soc.* **473**, 3051 (2018).
- [87] R. E. Smith, J. A. Peacock, A. Jenkins, S. D. M. White, C. S. Frenk, F. R. Pearce, P. A. Thomas, G. Efstathiou, and H. M. P. Couchman (VIRGO Consortium Collaboration), *Mon. Not. R. Astron. Soc.* **341**, 1311 (2003).
- [88] J. Liu, S. Bird, J. M. Z. Matilla, J. C. Hill, Z. Haiman, M. S. Madhavacheril, A. Petri, and D. N. Spergel, *J. Cosmol. Astropart. Phys.* **03** (2018) 049.
- [89] W. E. Schaap and R. van de Weygaert, *Astron. Astrophys.* **363**, L29 (2000).
- [90] M. C. Cautun and R. van de Weygaert, [arXiv:1105.0370](https://arxiv.org/abs/1105.0370).
- [91] H. Y. Wang, H. J. Mo, Y. P. Jing, Y. C. Guo, F. C. v. d. Bosch, and X. H. Yang, *Mon. Not. R. Astron. Soc.* **394**, 398 (2009).
- [92] J. C. Munoz-Cuartas, V. Mueller, and J. Forero-Romero, *Mon. Not. R. Astron. Soc.* **417**, 1303 (2011).
- [93] A.-S. Deutsch, E. Dimastrogiovanni, M. C. Johnson, M. Münchmeyer, and A. Terrana, *Phys. Rev. D* **98**, 123501 (2018).
- [94] J. Stücker, R. E. Angulo, and P. Busch, *Mon. Not. R. Astron. Soc.* **508**, 5196 (2021).
- [95] W. Briggs, V. Henson, and S. McCormick, *A Multigrid Tutorial*, 2nd ed. (SIAM, 2000).
- [96] W. H. Press, S. A. Teukolsky, W. T. Vetterling, and B. P. Flannery, *Numerical Recipes 3rd Edition: The Art of Scientific Computing*, 3rd ed. (Cambridge University Press, USA, 2007).
- [97] J. Hollowed, [arXiv:1906.08355](https://arxiv.org/abs/1906.08355).